Raman and infrared spectroscopic investigations of a ferroelastic phase transition in Ba_2ZnTeO_6 double perovskite

Roberto L. Moreira,[1,*] Ricardo P. S. M. Lobo,[2,3] Sérgio L. L. M. Ramos,[4] Mailadil T. Sebastian,[5] Franklin M. Matinaga,[1] Ariete Righi,[1] and Anderson Dias[6]

[1]*Departamento de Física, ICEx, Universidade Federal de Minas Gerais, C.P. 702, 30123-970 Belo Horizonte (MG), Brazil*
[2]*LPEM, ESPCI Paris, PSL University, CNRS, F-75005 Paris, France*
[3]*Sorbonne Université, CNRS, LPEM, F-75005 Paris, France*
[4]*Centro de Tecnologia em Nanomateriais (CT Nano), Universidade Federal de Minas Gerais, 30161-970 Belo Horizonte (MG), Brazil*
[5]*Materials Science and Technology Division, National Institute for Interdisciplinary Science and Technology, Trivandrum, Kerala 695019, India*
[6]*Departamento de Química, Universidade Federal de Ouro Preto, Campus Morro do Cruzeiro, ICEB II, 35400-000 Ouro Preto (MG), Brazil*

(Received 5 February 2018; published 16 May 2018)

The low-temperature vibrational properties of Ba_2ZnTeO_6 double-perovskite ceramics obtained by the solid-state route were investigated by Raman scattering and Fourier-transform infrared reflectivity. We found that this material undergoes a reversible ferroelastic phase transition at around 140 K, well compatible with a recently proposed rhombohedral-to-monoclinic structural change that would occur below 165 K. Complementary calorimetric measurements showed that the phase transition has a first-order character, with an entropy jump compatible with a displacive mechanism. The vibrational spectra show clearly the splitting of the doubly degenerate E modes into nondegenerate representations of the low-symmetry phase. In particular, the lowest-frequency Raman mode presents soft-mode behavior and splits below the critical temperature, confirming the in-plane ferroelastic deformation in the low-temperature phase.

DOI: 10.1103/PhysRevMaterials.2.054406

I. INTRODUCTION

Perovskite oxides are the most celebrated category among inorganic materials due to the ease with which the ABO_3 structures can accommodate different combinations of cations in the A and B sites. As a direct consequence, these materials present a large variety of physical properties and derived applications, going from piezoelectric, pyroelectric, and magnetoresistance transducers, catalysts, and solid oxide fuel cells, to ferroelectrics, multiferroics, and superconductors [1–9]. In fact, the multiple possibilities of random or ordered co-occupations of the A and B sites allow hundreds of compositions of tailored perovskite-related compounds to be achieved [9]. In particular, for a perfectly ordered $A_2B'B''O_6$ double perovskite, the B' and B'' cations occupy the octahedral sites in alternation, so that each $B'O_6$ octahedron is surrounded by six $B''O_6$ octahedra, and vice versa [10]. These materials usually crystallize into subgroups of the $Fm\bar{3}m$ cubic parent phase. However, in the case in which the A cation becomes too large and Goldsmith's tolerance factor becomes larger than 1, less common hexagonal structures related to h-$BaTiO_3$ occasionally become stable [9,10]. This appears to be the case of Ba_2ZnTeO_6, a double-perovskite whose structure and physical properties have been poorly explored so far, and which we investigated using vibrational spectroscopic techniques.

At room temperature, Ba_2ZnTeO_6 (BZT) belongs to a trigonal structure of the $R\bar{3}m$ space group [11], being isostructural to Ba_2NiTeO_6 (BNT) [12] and Ba_2TiMnO_6 (BTM) [13,14]. Although these materials are structurally stable, it has been recently shown that when treated at high pressures they undergo (nonreversible) polymorphic transformations to a different hexagonal $P6_3/mmc$ (BNT and BTM) or cubic $Fm\bar{3}m$ (BZT) structure [10]. $P6_3/mmc$ is also the ambient pressure structure of Ba_2CoSbO_6 (BCS) [15], which in turn shows a pressure-induced polymorphic transformation to the parent $Fm\bar{3}m$ structure [10]. The hexagonal $P6_3/mmc$ structure is also observed in other $Ba_2B'B''O_6$ ordered perovskites, such as Ba_2FeSbO_6 [15], Ba_2CrMoO_6 [16], and possibly Ba_2RhSbO_6 [17]. Other trigonal structures were found in several Ba-containing double perovskites: partially disordered $Ba_2Fe_{1.12}Os_{0.88}O_6$ and Ba_2ScRuO_6 (BSR) were recently shown to present the $P\bar{3}m1$ structure [18,19], the same structure proposed long ago to describe Ba_2NiReO_6 [20], Ba_2InRuO_6 [21], Ba_2NiOsO_6 and Ba_2CoOsO_6 [22], and Ba_2CoTeO_6 (BCT) [23]. However, more recent results showed that BCT is more likely to belong to the (ordered) trigonal $P\bar{3}m$ space group [24,25]. It is worth noticing that, at higher pressures, BSR presents a polymorphic transformation from the trigonal $P\bar{3}m1$ to the cubic $Fm\bar{3}m$ structure [19].

In addition to the already mentioned BZT, BNT, BTM, BCS, and BSR materials, which undergo pressure-induced polymorphic transformations, other barium- or lead-containing double perovskites exhibiting hexagonal structures show a very rich sequence of reversible structural phase transitions

*Author to whom all correspondence should be addressed: bmoreira@fisica.ufmg.br

(SPTs). This is the case, for instance, of Ba_2BiSbO_6, which for increasing temperature shows the structural sequence $I2/m \rightarrow R\bar{3} \rightarrow Fm\bar{3}m$ [26,27], and Ba_2LaTaO_6, whose SPT sequence is $P2_1/n \rightarrow I2/m \rightarrow R\bar{3}$ [28]. The sequence shown by $Ba_2Bi^{III}Bi^{V}O_6$ (BBB) is still more interesting, because in comparison with the two previous materials, it shows the complete SPT sequence with the four involved phases: $P2_1/n \rightarrow I2/m \rightarrow R\bar{3} \rightarrow Fm\bar{3}m$ [26]. Hexagonal lead-based materials show similar SPTs to the Ba-based ones. For increasing temperature, Pb_2MgTeO_6 shows the sequence $R\bar{3} \rightarrow Fm\bar{3}m$ [29]; Pb_2CoTeO_6 (PCT) transforms as $P2_1/n \rightarrow I2/m \rightarrow R\bar{3} \rightarrow Fm\bar{3}m$ [30]; and Pb_2TmSbO_6 as $C2/c \rightarrow P2_1/n \rightarrow R\bar{3} \rightarrow Fm\bar{3}m$ [31]. Notice that PCT presents the same SPT sequence of BBB.

In recent works, the interplay between the structural and magnetic properties of Ba_2MTeO_6 (M = Ni, Cu, and Zn) below room temperature has been explored [32,33]. In those works, the authors claim that, while the $R\bar{3}m$ rhombohedral structure of BNT remained stable down to 1.8 K, Ba_2CuTeO_6 (BCuT) presented a SPT from a room-temperature monoclinic ($C2/m$) to a triclinic ($P\bar{1}$) structure below 287 K. In addition, BZT would also present a SPT below 165 K, from the room-temperature $R\bar{3}m$ phase to a $C2/m$ monoclinic one. As introduced in the previous paragraphs, hexagonal double-perovskites show a variety of structural phases and temperature- or pressure-induced SPT. The proposed $R\bar{3}m$ to $C2/m$ SPT for BZT appears as a new possibility of symmetry lowering for such systems, which deserves to be investigated in detail. Indeed, as noticed by Gibbs *et al.* [32], if the $C2/m$ phase holds for the nonmagnetic BZT, then what is the contribution of the Jahn-Teller effect of the Cu^{2+} ion on the distorted structures of BCuT? Therefore, in order to contribute to the debate about the structural stability of BZT and to bring new useful information about the lattice-dynamics behavior of rhombohedral and monoclinic Ba_2MTeO_6 compounds, we have undertaken systematic low-temperature Raman and infrared-reflectivity experiments on Ba_2ZnTeO_6 ceramic samples. A SPT of a ferroelastic nature was found at around 140 K, which can be identified with that claimed by Gibbs *et al.* [32]. The spectroscopic data are analyzed within the framework of group theory and supported by calorimetric and diffractometric measurements.

II. METHODS

Ba_2ZnTeO_6 ceramics were prepared using the solid-state ceramic route. High-purity $BaCO_3$, ZnO, and TeO_2 (Sigma-Aldrich, purity >99.9%) were used as starting materials. Stoichiometric amounts of the powder mixtures were ball-milled in distilled water as a medium, for 24 h, using yttria-stabilized zirconia in a plastic container. The slurry was dried, ground well, and slowly heated (2.5 °C/min) in air up to 750 °C and kept for 4 h at this temperature to allow the complete oxidation of Te^{4+} to Te^{6+} [34,35]. The mixed powders were subsequently calcined at 1050 °C for 4 h and reground at room temperature. To improve the sinterability of Ba_2ZnTeO_6, 0.2 wt. % of B_2O_3 was added to the powders as sintering aids. After regrinding, the powders were mixed to 4 wt. % of polyvinyl alcohol (binder), dried, and ground well again. Cylindrical pucks (13 mm diameter and 10 mm height) were prepared at 150 MPa. These compacts were heated to 600 °C (30 min) to expel the binder, and then sintered at 1125 °C for 2 h. The crystal structure of the samples was studied by x-ray diffraction (XRD) using a PANalytical-EMPYREAN diffractometer with a double-Ge monochromator in the 15°–140° 2θ range (continuous scanning, step size of 0.0263° 2θ, counting time 100 s), operating with a Cu anode, 45 kV and 40 mA. The software MDI Jade 9.0 was employed to calculate the lattice parameters. Differential scanning calorimetry (DSC) measurements were performed with Perkin-Elmer DSC8000 equipment on calcined powders (17 mg) from 100 to 300 K during cooling and heating cycles with 5–20 K/min rates under an He atmosphere.

Sintered samples were polished to an optical grade (0.25 μm) and subjected to spectroscopic measurements. Micro-Raman spectra were collected in a backscattering configuration in three different spectrometers (Horiba/Jobin-Yvon LABRAM-HR, Horiba/Jobin-Yvon T64000, and WITec Alpha300R), using appropriate confocal microscopes, diffraction gratings (600, 1800, and 2400 grooves/mm), and CCD (charge-coupled device) detectors. Polarized Raman experiments were performed on the LABRAM spectrometer using a 632.8 nm laser line, 100 × objective, and 6 mW at the surface of the sample. The low-temperature measurements were done either on the T64000 triple-monochromator (532 nm excitation line, 20 × objective, 8 mW at the surface of the sample, and Janis cryostat) from 50 to 300 K in the 60−1000 cm^{-1} region; or on a WITec spectrometer [532 nm laser line, volume Bragg grating (VGB) notch filter, 50 × objective, 1.5 mW at the surface of the sample, and Linkam/THMS600 cryostat] in the low-frequency region (down to 10 cm^{-1}). Up to four collections of 50 s were accumulated for statistical improvement, and the spectral resolutions were better than 1 cm^{-1}.

Low-temperature (5–300 K) infrared reflectivity spectra were recorded during the heating cycles in a Fourier-transform spectrometer (Bruker IFS 66V) equipped with a home-made specular reflectance accessory (incidence angle of 11.5°). In the midinfrared region (500−2500 cm^{-1}) we used a SiC globar lamp as an infrared source, a Ge-coated KBr beamsplitter, and an LN_2-cooled Si:B photodetector. In the far-infrared range (30−700 cm^{-1}), we employed a mercury-arc lamp, a 6 μm Ge coated Mylar beamsplitter, and an LHe-cooled Si:B bolometer. *In situ* (inside an ARS Hetran cryostat) evaporated gold [36] onto the sample surface was used as a reference. For each spectral region, the measurements were performed in two complete temperature cycles: initially, the spectra were collected using a stainless-steel mirror as a reference; subsequently, gold was evaporated on the sample surface, and the spectra of this gold-coated sample were collected at the same temperatures, using the same stainless mirror as a reference; finally, the spectra of the first cycle were divided by the corresponding ones of the second cycle in order to correct for losses due to sample geometry, rugosity, etc. The data were collected by averaging at least 256 scans, and the frequency resolution was typically 2 cm^{-1}. The reflectivity spectra were evaluated by standard Kramers-Krönig (KK) analysis and adjusted by a Lorentz-based oscillator model.

TABLE I. Factor-group analysis for the room-temperature rhombohedral room-temperature phase of Ba_2ZnTeO_6, based on the Wyckoff positions of isostructural Ba_2NiTeO_6 [12].

Atom	Wyckoff site	Symmetry	Irreducible representations (IRs)
		Rhombohedral $R\bar{3}m$ $(\text{no.}166, D_{3d}^5)$	
Ba(1)	$6c$	C_{3v}	$A_{1g} + A_{2u} + E_g + E_u$
Ba(2)	$6c$	C_{3v}	$A_{1g} + A_{2u} + E_g + E_u$
Zn	$6c$	C_{3v}	$A_{1g} + A_{2u} + E_g + E_u$
Te(1)	3^a	D_{3d}	$A_{2u} + E_u$
Te(2)	$3b$	D_{3d}	$A_{2u} + E_u$
O(1)	$18h$	C_s	$2A_{1g} + A_{1u} + A_{2g} + 2A_{2u} + 3E_g + 3E_u$
O(2)	$18h$	C_s	$2A_{1g} + A_{1u} + A_{2g} + 2A_{2u} + 3E_g + 3E_u$
		$\Gamma_{\text{total}} = 7A_{1g} + 2A_{2g} + 9E_g + 2A_{1u} + 9A_{2u} + 11E_u$, $\Gamma_{\text{silent}} = 2A_{2g} + 2A_{1u}$	
		$\Gamma_{\text{acoustic}} = A_{2u} + E_u$, $\Gamma_{\text{Raman}} = 7A_{1g} + 9E_g$ and $\Gamma_{\text{infrared}} = 8A_{2u} + 10E_u$	

III. RESULTS AND DISCUSSIONS

A. Room-temperature analysis

XRD data confirmed that crystalline, single-phase Ba_2ZnTeO_6 (BZT) double perovskites were obtained, with no secondary phases or impurities detected. A typical XRD for BZT with Miller indices for the main Bragg peaks is presented in Fig. S1 of the Supplemental Material (SM) [37]. The indexation was performed according to the proposed trigonal structure of BZT, within the $R\bar{3}m$ space group [11,32], and by comparison with the no. 25005-ICSD file of the FIZ-Karlsruhe center of the isostructural Ba_2NiTeO_6 (BNT) compound [12]. The indexation was very good, and the obtained lattice parameters were $a = 5.83$ Å and $c = 28.77$ Å of the $R\bar{3}m$ (no. 166) rhombohedral space group, with six formula units ($Z = 6$), well compatible with previously reported data for BZT [10,11]. Thanks to the good agreement between structural data of BZT and BNT, we took the Wyckoff positions determined for BNT [12] and the nuclear site method of Rousseau *et al.* [38] to predict the number, selection rules, and symmetries of the vibrational modes of BZT at room temperature. The results are presented in Table I. This procedure predicts 16 Raman ($7A_{1g} + 9E_g$) and 18 infrared ($8A_{2u} + 10E_u$) modes for the room-temperature structure of BZT (belonging to the $R\bar{3}m$ space group). These predictions were used to analyze the optical vibrational data.

Figure 1 presents the room-temperature infrared spectra of BZT. From top to bottom, the three panels present (a) the reflectivity, and (b) and (c) the KK calculated real and imaginary parts of the infrared dielectric function. Close to normal incidence, the infrared reflectivity and the complex dielectric function are related by the Fresnel formula [39,40]:

$$R(\omega) = \left| \frac{1 - \sqrt{\tilde{\varepsilon}(\omega)}}{1 + \sqrt{\tilde{\varepsilon}(\omega)}} \right|^2, \quad (1)$$

and the dielectric function can be described by the usual sum of Lorenz oscillators, i.e.,

$$\tilde{\varepsilon}(\omega) = \varepsilon(\infty) + \sum_j \frac{\Delta\varepsilon_j \Omega_{\text{TO}j}^2}{\Omega_{\text{TO}j}^2 - \omega^2 - i\gamma_j\omega}. \quad (2)$$

In the above equation, Ω_j and γ_j are the frequency and damping constants of the transversal (TO) branch of the jth mode, $\Delta\varepsilon_j$ is the dielectric strength of the corresponding mode, and $\varepsilon(\infty)$ accounts for vacuum and electronic polarization contributions.

To obtain the polar phonon-dispersion parameters with higher accuracy, we have performed a fit of the imaginary part of the KK obtained dielectric constant [Fig. 1(c)] with Eq. (2). Then, the obtained parameters were used to calculate the infrared reflectivity and the dielectric spectra [Eqs. (1) and (2)], in very good agreement to the experimental data [Figs. 1(a) and 1(b)]. All of the 18 polar phonon modes expected at room temperature were identified, although this procedure alone does not allow identifying the symmetries of the modes.

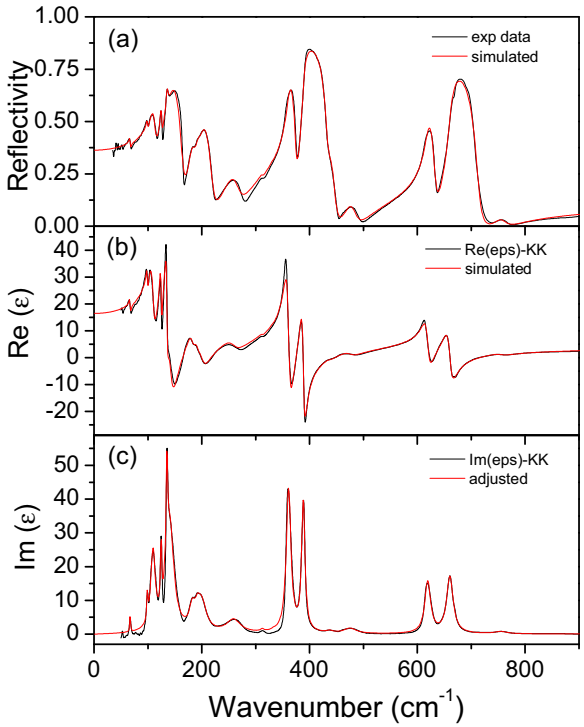

FIG. 1. (a) Experimental infrared reflectivity spectra and the KK calculated (b) real and (c) imaginary parts of the dielectric constant of BZT at room temperature. In (c) the adjusted spectrum is also presented for $\varepsilon''(\omega)$. In (a) and (b) the experimental data are presented besides the simulated ones, obtained with the fitting parameters of $\varepsilon''(\omega)$.

TABLE II. Polar phonon-dispersion parameters for Ba_2ZnTeO_6 at 5 and 300 K. Wave numbers (Ω) and damping constants (γ) are in cm^{-1}, and the dielectric strengths are dimensionless. The tentative assignments were done by checking the modes that split in the low-temperature phase (degenerate room-temperature modes) and those that appear in that phase (silent at room temperature). The assignments of modes above 350 cm^{-1} also reference the findings of Ref. [41]. ε_∞ and ε_0 are the extrapolated (real) dielectric constants, when $\omega \to \infty$ and $\omega \to 0$, respectively.

		5 K			300 K			
No.	LT IR	$\boldsymbol{\Omega_{TO}}$	$\boldsymbol{\gamma_{TO}}$	$\Delta\varepsilon$	$\boldsymbol{\Omega_{TO}}$	$\boldsymbol{\gamma_{TO}}$	$\Delta\varepsilon$	RT IR
1	$A_u + B_u$	63.0	3.1	0.272	67.1	1.8	0.122	E_u
1′		71.7	3.0	0.420				
2	B_u	100.4	2.6	0.544	99.0	2.4	0.181	A_{2u}
3	$A_u + B_u$	105.0	3.0	0.100	109.6	10.2	2.125	E_u
3′		109.6	10.3	3.270				
4	$A_u + B_u$	122.0	2.0	0.307	124.5	2.8	0.446	E_u
4′		128.2	1.8	0.292				
5	$A_u + B_u$	133.7	2.5	0.853	135.2	4.5	1.070	E_u
5′		139.2	2.5	0.396				
6	B_u	143.0	16.5	3.916	141.6	17.9	3.508	A_{2u}
7	B_u	183.7	10.0	0.486	182.2	12.3	0.387	A_{2u}
8	B_u	193.4	7.6	0.388	192.1	12.9	0.307	A_{2u}
9	B_u	201.0	14.3	0.709	200.6	20.5	0.824	A_{2u}
(sil.)	A_u	231.0	7.5	0.031				A_{1u}
10	$A_u + B_u$	251.0	23.2	0.300	259.5	31.9	0.457	E_u
10′		266.0	20.0	0.300				
11	$A_u + B_u$	310.0	3.2	0.014	312.1	7.6	0.016	E_u
11′		314.5	3.0	0.010				
(sil.)	A_u	331.5	4.1	0.006				A_{1u}
12+12′	$A_u + B_u$	358.9	9.6	1.475	361.2	10.4	1.150	(E_u)[a]
13+13′	$A_u + B_u$	386.9	6.0	0.774	388.4	7.5	0.765	(E_u)[a]
14	B_u	438.5	9.6	0.008	437.5	14.9	0.019	A_{2u}
15	B_u	476.0	30.0	0.102	475.4	28.5	0.090	A_{2u}
16	$A_u + B_u$	613.0	8.7	0.127	619.2	13.7	0.333	(E_u)[a]
16′		621.3	10.6	0.239				
17	$A_u + B_u$	660.0	9.4	0.170	660.4	13.2	0.347	(E_u)[a]
17′		664.3	7.0	0.127				
18	B_u	761.5	21.4	0.025	755.3	30.1	0.026	A_{2u}
		$\varepsilon_0 = 19.61$; $\varepsilon_\infty = 3.95$			$\varepsilon_0 = 16.28$; $\varepsilon_\infty = 4.10$			

[a](E_u) modes according to Corsmit and Blassein (BNT [41]).

The room-temperature infrared dispersion parameters found for BZT, including the extrapolated infinity (ε_∞) and static ($\varepsilon_0 = \varepsilon_\infty + \Sigma_j \Delta\varepsilon_j$) dielectric constants, are presented in the right columns of Table II. This table also presents the low-temperature (LT) polar phonon-dispersion parameters and the tentative assignment of symmetries of room-temperature (RT) polar phonons, which will be discussed in more detail in the next section. The results presented in Table II extend substantially our knowledge on the polar phonon behavior of BZT (and isostructural BNT) in the rhombohedral phase, since just transmission spectra above 350 cm^{-1} were available so far [11,41], reporting only the eight higher-frequency modes. Despite that, the symmetries of modes at 361 and 388 cm^{-1} (TeO_6 deformations) and 619 and 660 cm^{-1} (TeO_6 stretching modes) have been correctly described for BNT [41] as belonging to the E_u irreducible representation (IR), helping us in our attribution of Table II.

Once we had obtained a very good agreement between predicted and observed infrared reflectivity spectra of BZT, Raman experiments were carried out on the ceramic samples, and the spectra collected at room temperature are presented in Fig. 2 for nonpolarized light (a) and polarized light (b). In Fig. 2(a), the nonpolarized spectrum was adjusted by 16 Lorentzian lines, in perfect agreement with group theory predictions for this material, in the rhombohedral $R\bar{3}m$ structure. Notice, in the inset of Fig. 2(a), the presence of a relatively low-frequency mode, around 30 cm^{-1} at room temperature, whose temperature behavior deserves special attention, as discussed later. Now, since well-sintered ceramic samples usually have micrometer grains, polarized Raman spectra with appropriate scattering geometries and high magnification objectives can bring additional information about both the presence of quasidegenerate modes and their likely symmetries [42,43]. In the present case, for the room-temperature D_{3d} point group, by scanning over the sample under the microscope, one expects to favor the A_{1g} modes when measuring with parallel-polarized light (the base functions for A_{1g} IR are $x^2 + y^2$ and z^2), and conversely to favor the E_g modes when collecting the spectra in a cross-polarized configuration (the E_g base functions are $x^2 - y^2$,xy,xz, and yz). The frequencies and damping

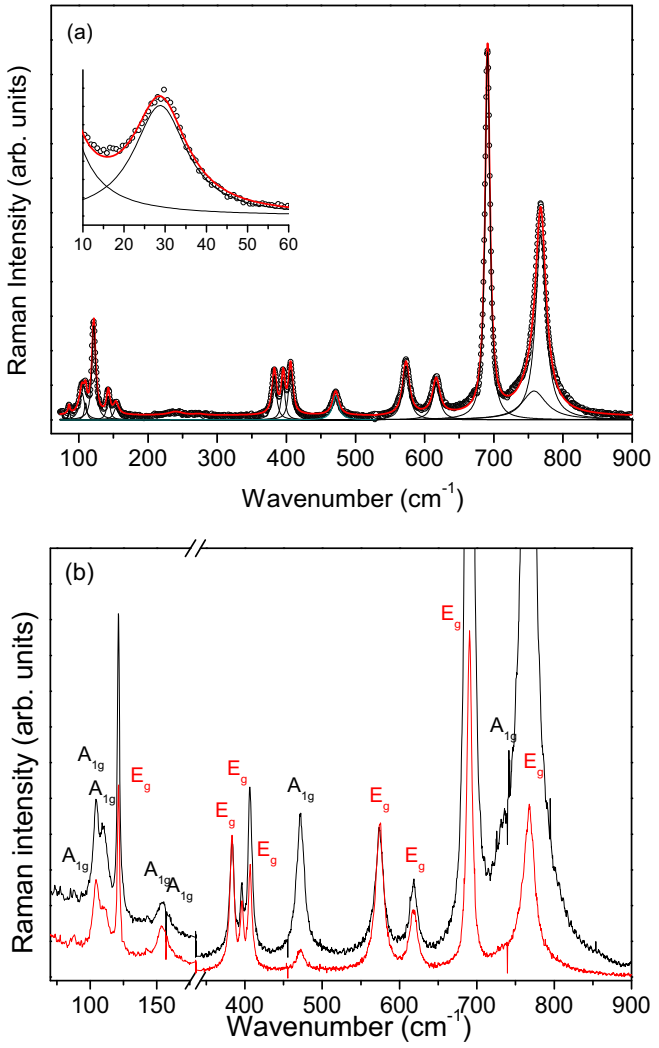

FIG. 2. (a) Room-temperature Raman spectrum of BZT obtained with nonpolarized light, adjusted by 16 Lorentzian lines. (b) Parallel-polarized (black line) and cross-polarized (red line) Raman spectra for BZT at room temperature, from 60 to 900 cm^{-1}, showing predominantly A_g and E_g modes, in each case.

constants of all the 16 discerned modes of BZT from the fitting procedures, along with the proposed symmetries at room temperature, are presented in the right side of Table III. This tentative assignment, by analysis of measured polarized Raman spectra, will be checked in comparison with low-temperature spectra in the next section. It is also worth mentioning that the present results confirm and extend the knowledge of Raman modes of BZT: indeed, we observed seven of the eight observed modes in Ref. [11] (one mode proposed at 373 cm^{-1} by those authors was not confirmed here). Therefore, as a whole, in our work, all the predicted optical vibrational modes (Raman and infrared) of BZT at room temperature were identified.

B. Low-temperature investigations

To check the already mentioned structural phase transition of BZT below room temperature and to investigate the behavior of phonon modes at low temperatures, Raman and infrared-reflectivity spectra of a ceramic sample were collected

TABLE III. Depicted Raman modes of Ba_2ZnTeO_6, at 50 and 300 K. Wave numbers (Ω) and full widths at half-maximum (FWHM) are in cm^{-1}. The tentative assignments were done by using polarized Raman spectra and by checking the modes that split in the low-temperature phase (degenerate E_g modes) and one new mode that appears below 140 K (silent A_{2g} mode), around 185 cm^{-1}.

		50 K		300 K		
No.	LT IR	Ω	FWHM	Ω	FWHM	RT IR
1	$A_g + B_g$	37.3[a]	4.0[a]	28.8	12.6	E_g
1′		50.7[a]	4.3[a]			
2	A_g	92.6	4.0	86.0	5.0	A_{1g}
3	A_g	99.4	4.0	104.3	9.2	A_{1g}
4	A_g	108.7	3.8	109.7	4.2	A_{1g}
5	$A_g + B_g$	119.1	3.4	121.4	6.3	E_g
5′		125.9	6.0			
6	A_g	140.6	2.5	142.5	5.7	A_{1g}
7	A_g	166.0	6.1	153.7	7.2	A_{1g}
(sil.)	B_g	184.8	8.0			A_{2g}
8	$A_g + B_g$	379.2	3.9	382.7	7.5	E_g
8′		382.2	4.2			
9	$A_g + B_g$	397.9	3.9	395.5	6.3	E_g
9′		399.9	2.9			
10	$A_g + B_g$	404.6	3.1	406.2	7.3	E_g
10′		406.6	2.8			
11	A_g	469.8	7.6	471.3	11.5	A_{1g}
12	$A_g + B_g$	574.2	4.6	572.0	11.7	E_g
12′		577.6	4.8			
13	$A_g + B_g$	615.9	4.9	616.0	13.1	E_g
13′		621.8	6.4			
14	$A_g + B_g$	693.6	3.4	690.8	8.5	E_g
14′		695.7	3.7			
15	A_g	756.1	40.8	756.1	45.4	A_{1g}
16	$A_g + B_g$	770.9	8.0	767.7	18.1	E_g
16′		773.3	5.6			

[a]Data obtained at 80 K.

in several temperature cycles and different spectrometers, from room temperature down to 5 K. As we will show in this section, a SPT clearly showed up, below 140 K, in all measurements. Before presenting the results, and in order to get more information on the type, character, and mechanism of the phase transition (besides critical temperatures, of course), calorimetric measurements (DSC) were performed on calcined BZT powder and the experimental results are shown in Fig. S2 of the SM [37]. The DSC data confirmed a SPT at around 140 K, with small entropy jump (0.03 R ln2), allowing us to characterize the structural change as a first-order one, with a displacive character [44], i.e., occurring due to the softening of a phonon mode. Therefore, we paid special attention to the low-frequency wave-number region in order to check on a possible soft-mode phonon behavior.

Figure 3(a) shows the low-temperature infrared-reflectivity data (here limited to the 40−750 cm^{-1} interval), from 5 to 300 K, during the heating run. It is possible to observe the doubling of some peaks below 140 K, particularly around 67, 110, 135, and 620 cm^{-1} (indicated by asterisks). Because the infrared reflectivity is not a linear superposition of contributions of individual excitations, the phonon changes during the SPT are better visualized in the low-temperature behavior

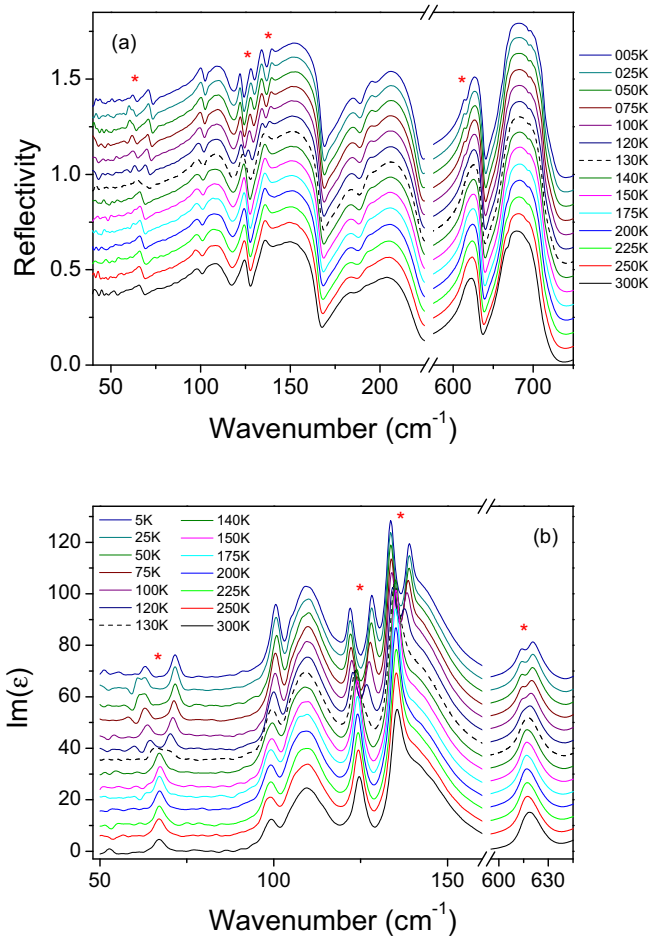

FIG. 3. (a) Infrared reflectivity and (b) KK calculated imaginary part of the dielectric constant of BZT from 5 to 300 K. The spectra have been vertically shifted for better visualization. Asterisks denote the splitting of degenerate E_u modes of the rhombohedral room-temperature structure. The spectra obtained at 130 K are presented in dashed lines because they show a mixture of low- and high-temperature phases.

of the imaginary part of the dielectric response, shown in Fig. 3(b).

In addition to showing a beautiful picture of the phonon-modes evolution, the peak splitting below 140 K seen in Fig. 3 is an indication of the raising of the degeneracy of the doubly degenerate E_u modes of the rhombohedral phase into nondegenerate modes of the lower-symmetry structure (monoclinic), well compatible with the ferroelastic SPT proposed for BZT ($\bar{3}mF2m$, in Aizu's classification of ferroelastic SPT) [45]. The subgroups of the $R\bar{3}m$ space group are $C2/m$ (monoclinic), $R\bar{3}$, $R32$, $R3m$, $P\bar{3}m1$, $R\bar{3}m$, and $R\bar{3}c$ (all trigonal). The splitting of the degenerate modes shown in our work has the characteristics of ferroic transitions. The transition could then be ferroelectric and/or ferroelastic. However, the static dielectric constant (measured here) did not show any divergence at the critical temperature; then, the transition is not ferroelectric, ruling out a transition to $R3m$ (C_{3v} point group). The phase transition is then ferroelastic, requiring a change of the crystal system and ruling out all rhombohedral groups to the LT phase. Hence, the only subgroup that remains is $C2/m$. Thus, assuming the monoclinic $C2/m$ (no. 12) structure as the correct one for the low-temperature phase of BZT, we can use group-to-subgroup relationships to look for the number, symmetries, and correlations between phonon modes of the two involved structural phases. Indeed, the Wyckoff positions of the ions must be correlated, so we used the following transformation rules connecting those positions [46]: $6c$, $3a$, and $3b$ of the D_{3d} group transform, respectively, into $4i$, $2a$, and $2b$ of the C_{2h} one; $6h$ of D_{3d} transforms into two inequivalent $4i$ and $8j$ positions of C_{2h}. With these new positions, factor group tools can be used to calculate the phonon-mode representation at the Brillouin-zone center for the low-temperature $C2/m$ monoclinic phase, as summarized in Table IV. These results show that 27 first-order Raman modes and 30 infrared ones would be active in the monoclinic low-temperature phase (notice that in this structure there are no silent modes).

Now, we can check how the phonon modes of both structures are correlated in this group-to-subgroup rhombohedral (R) to monoclinic (M) SPT. Indeed, the *gerade* modes of these structures are correlated as follows (always in the order R to M): the $7A_{1g}$ transforms into $7A_g$; the $2A_{2g}$ silent modes activate into $2B_g$; the nine degenerate E_g modes split into $9A_g + 9B_g$ modes. For the *ungerade* modes, the correlations are as follows: the $9A_{2u}$ modes transform into $9B_u$ ones; the $2A_{1u}$ (silent)

TABLE IV. Factor-group analysis for the proposed low-temperature monoclinic phases of Ba_2ZnTeO_6 [32,33]. The Wyckoff positions are those compatible with a group-to-subgroup phase transition [45].

Atom	Wyckoff site	Symmetry	Irreducible representations (IRs)
		Monoclinic $C2/m$(no. 12,C_{2h}^3)	
Ba(1)	$4i$	C_s	$2A_g + A_u + B_g + 2B_u$
Ba(2)	$4i$	C_s	$2A_g + A_u + B_g + 2B_u$
Zn	$4i$	C_s	$2A_g + A_u + B_g + 2B_u$
Te(1)	$2a$	C_{2h}	$A_u + 2B_u$
Te(2)	$2b$	C_{2h}	$A_u + 2B_u$
O(1)	$4i$	C_s	$2A_g + A_u + B_g + 2B_u$
O(2)	$8j$	C_1	$3A_g + 3A_u + 3B_g + 3B_u$
O(3)	$4i$	C_s	$2A_g + A_u + B_g + 2B_u$
O(4)	$8j$	C_1	$3A_g + 3A_u + 3B_g + 3B_u$
		$\Gamma_{\text{total}} = 16A_g + 11B_g + 13A_u + 20B_u$, $\Gamma_{\text{acoustic}} = A_u + 2B_u$	
		$\Gamma_{\text{Raman}} = 16A_g + 11B_g$ and $\Gamma_{\text{infrared}} = 12A_u + 18B_u$	

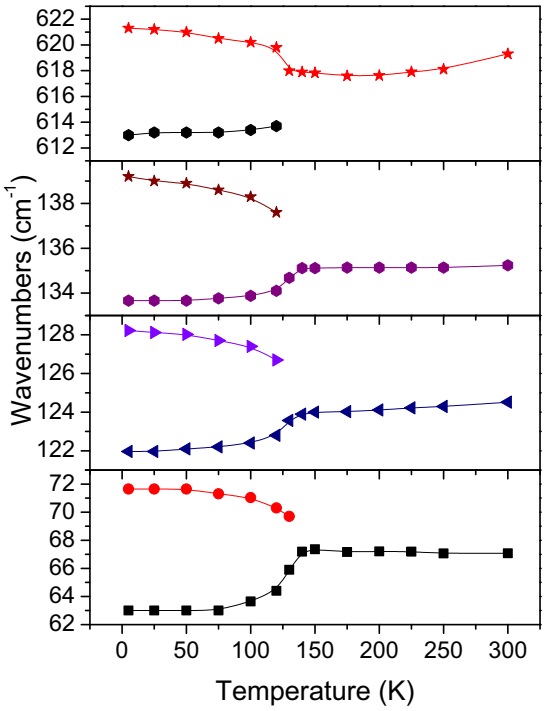

FIG. 4. Temperature evolution of the phonon frequencies of the E_u infrared modes around 67 cm^{-1} (peak 1, in Table II), 124.5 cm^{-1} (peak 4), 135 cm^{-1} (peak 5), and 619 cm^{-1} (peak 16), showing the peak doubling due to the ferroelastic transition below 140 K.

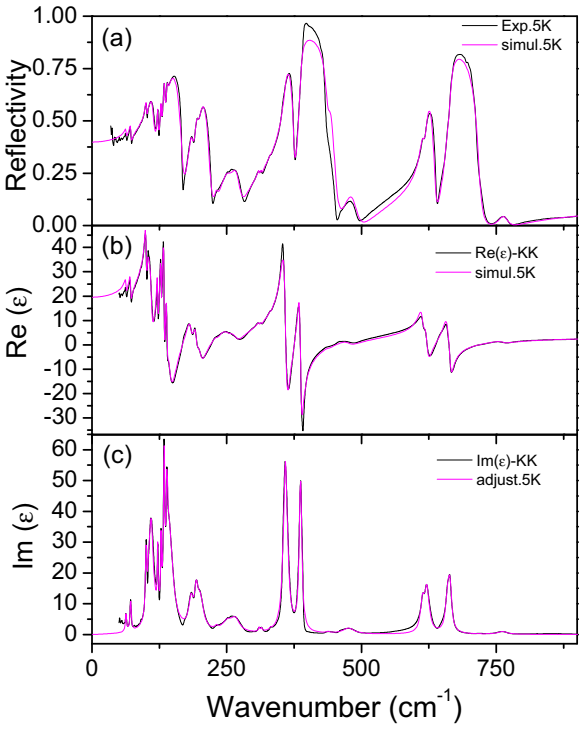

FIG. 5. (a) Experimental and simulated infrared reflectivity spectra for BZT at 5 K; (b) and (c) the KK calculated (b) real and (c) imaginary parts of the dielectric constant at 5 K, along with the simulated (b) and adjusted (c) corresponding spectra.

modes into $2A_u$; the $11E_u$ modes split into $11A_u + 11B_u$ modes. These results are in agreement with Table IV, and they show how to interpret the peak splitting from the *R*-to-*M* SPT: we would expect to see the 9 E_g and the 10 infrared-active E_u modes of the room-temperature structure duplicating into the corresponding nondegenerate IR of the low-temperature phase.

The low-temperature Im(ε) spectra of Fig. 3(b) were adjusted by Eq. (2). Above 140 K, the spectra were fitted with 16 modes; below this temperature, 28 phonons were necessary for properly adjusting the spectra. The temperature evolution of the peak positions (phonon wave numbers) of all polar modes are presented in Figs. S3(a)–S3(d) of the SM [37]. In general, the phonon modes are well behaved within each structural phase, showing a slight hardening upon decreasing temperature. The most interesting results are the splitting of eight "bands" (raising of the degeneracy of E_u modes) and the activation of the two (A_{1u}) silent modes that occur at the SPT (Fig. S3) [37]. The splitting of the four highlighted modes of Fig. 3 (indicated by asterisks) is displayed in detail in Fig. 4. The phonon-mode behavior shown by these (E_u-type) modes around the phase transition (Fig. 4) is well compatible with the first-order ferroelastic SPT proposed for the material (the frequency difference of the split modes did not seem to vanish at the phase transition; the doubling of the E_u modes is compatible with the appearance of an in-plane elastic deformation).

The fittings of the Im(ε) functions give us all the relevant dispersion parameters of BZT into the low-temperature phase. To validate the adjustments, we show in Fig. 5 the measured infrared reflectivity and the KK-calculated real and imaginary parts of the dielectric constant, at 5 K, besides the indicated adjusted [Im(ε)] and simulated [reflectivity and Re(ε)] spectra. The goodness of the theoretical curves is quite clear. The obtained fitting parameters are presented in Table II (left columns). Notice in this table that, by using the observed peak splitting and the correlation between the IR of both phases, the assignment of the polar modes at room temperature could be done. Only two modes that would have E_u symmetry did not split at low temperature. However, according to Ref. [41], these would be modes number 12 and 13. Therefore, taking this information into account, all infrared modes of the rhombohedral room-temperature phase could be identified and assigned to their respective symmetries. Concerning the low-temperature phase, taking into account that the phonons $12+12'$ and $13+13'$ present quasiaccidental degeneracy (they are so close in frequency that they cannot be discerned in nonpolarized measurements in polycrystals), we can also say that all frequencies of the polar modes have been determined for the monoclinic phase. However, concerning the phonon symmetries within this phase, we were only able to present a partial assignment, as shown in Table II.

Let us now move to the low-temperature Raman spectra of BZT. The four panels of Fig. 6 show the drastic changes in the Raman spectra of the material accompanying the structural change: peak splitting (due to the raising of the degeneracy of E_g modes), a new peak (activation of one silent mode), and, more spectacularly, the behavior of the lowest-frequency Raman mode [see Fig. 6(a)], which is addressed first. Indeed, this mode presents clear soft-mode behavior, its frequency

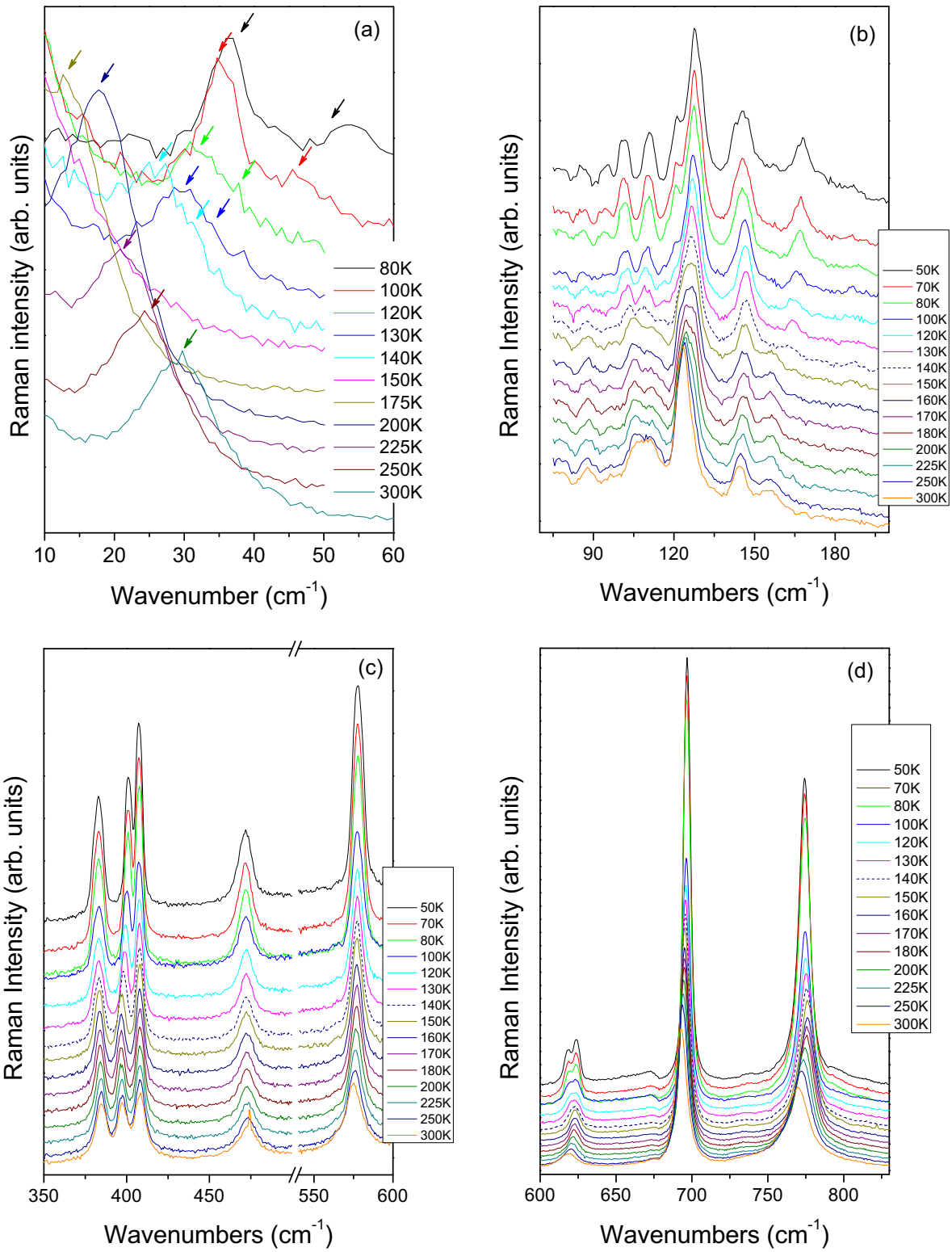

FIG. 6. Low-temperature Raman spectra around the ferroelastic phase transition of BZT. Panel (a) shows detail focusing on the raising of degeneracy and the *soft-mode* behavior of the lowest-frequency (no. 1) E_g mode. Single asterisks denote the softening of the $E_g(1)$ mode on cooling; double asterisks denote the softening of $A_g(1) + B_g(1')$ modes, on heating. Panels (b), (c), and (d) show the temperature evolution of the *hard* phonons in the frequency regions $60-200\,\mathrm{cm}^{-1}$ (features 2–7), $350-600\,\mathrm{cm}^{-1}$(features 8–12), and $600-850\,\mathrm{cm}^{-1}$ (features 13–16), respectively.

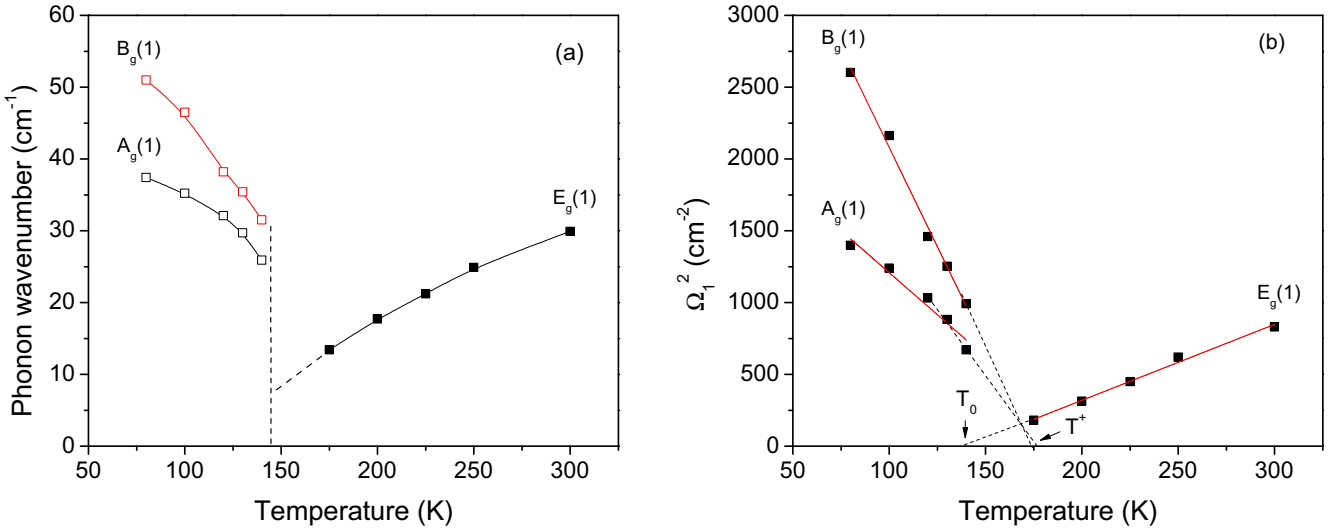

FIG. 7. Temperature behavior of (a) the soft-mode frequency (Ω_1) and (b) the square of this phonon frequency in the region around the low-temperature phase transition. T_0 and T^+ are the stability limits of the paraelastic and ferroelastic phases, respectively.

going to zero when approaching the critical temperature (around 140 K). Upon cooling below this temperature, the frequency starts increasing and this peak doubles. Therefore, we can say that (i) this is the phonon mode that drives the displacive SPT; (ii) the lowest-frequency Raman mode is an E_g-rhombohedral mode, which we will call $E_g(1)$; (iii) the $E_g(1)$ mode splits the low-temperature monoclinic phase into two modes, $A_g(1) + B_g(1')$.

In displacive-type transitions, the soft mode always belongs to a Raman-active totally symmetric IR of the lower-symmetry phase (here, A_g), a claim that is known as Worlock's conjecture [47]. In the present case, since the SPT leads to the appearance of a (ferro)elastic deformation (i.e., deformation into the rhombohedral ab plane), a mode linked to indistinguishable rhombohedral x and y base functions should be the soft mode (i.e., an E_g-type mode). Moreover, since the number of motifs is the same for the high- and low-temperature primitive cells, the condensation of the soft-mode must occur at the center of the Brillouin zone, and thus the soft mode must be seen in both phases. The fact that a B_g-type mode (no. $1'$) also presented soft-mode behavior can be explained because its origin is the same as that of $A_g(1)$, i.e., both originate from $E_g(1)$. This situation is analogous to the soft-mode behavior of the $E_g(1)$ mode in tetragonal $SrTiO_3$—in the paraelectric-to-ferroelastic transition of this material, the expected soft mode is $A_{1g}(1)$, which is derived from a triply degenerate $F_{2u}(1)$ mode, which, in that SPT, splits into $A_{1g}(1) + E_g(1)$ [48]. In both cases, Worlock's conjecture remains valid and the low-temperature phases of the materials present twin soft modes belonging to orthogonal IR.

The three other panels of Fig. 6 show the temperature behavior of the *hard* Raman modes in the frequency regions 60−180 cm^{-1} (panel b, features 2–7 of Table III), 350−600 cm^{-1} (panel c, features 8–12), and 600−850 cm^{-1} (panel d, modes 13–16). In particular, we can observe the splitting of some E_g modes at around 121 and 616 cm^{-1}, for instance the upshift of the mode around 153 cm^{-1} and the appearance of a new mode around 185 cm^{-1} below 140 K. To make a more quantitative analysis of the low-temperature evolution of the Raman spectra of BZT, we have used peak fitting procedures (Lorentzian lines) to depict the relevant *gerade* modes of BZT in the temperature range 50–300 K. The results can be seen in Figs. S4a–S4c of the SM [37], which give the phonon frequencies for all depicted Raman modes from 50 to 300 K. A summary of the fitting parameters (frequencies and damping constants) of the Raman spectrum obtained at 50 K is presented in the left columns of Table III. Analogous to the previous case of the polar modes, we were able to find the Raman modes that split at the phase transition, i.e., the E_g modes that transform into $A_g + B_g$, confirming the attributions of the polarized measurements. The seven room-temperature A_{1g}-type modes evolve to seven A_g modes of the low-temperature phase. One silent mode (formerly, an A_{2g} mode) seems to activate in the low-temperature phase at around 185 cm^{-1}, being identified as a new B_g monoclinic mode.

The temperature behavior of the lowest-frequency mode (the soft mode) gives useful information about the phase transition. Indeed, this mode usually softens as $|T–T^*|^{1/2}$, where T^* is a critical temperature, because of its dependence with the primary order parameter (here, the in-plane elastic deformation would be the macroscopic order parameter), in group-to-subgroup Landau-type transitions [49]. Thus, we plotted, in Fig. 7(a), the temperature evolution of the soft-mode around the ferroelastic transition (dashed lines are extrapolation end limits of the SPT), and, in Fig. 7(b), the square of the frequency of the soft mode(s) as a function of the temperature. The second plot shows clearly some linear tendencies and, by extrapolation, the stability limits of the paraelastic phase (T_0, around 140 K) and that of the ferroelastic phase (T^+, around 175 K). These results confirm the first-order character of the SPT. They also give an idea of the maximum possible thermal hysteresis ($4/3 \times \Delta T = T^+–T_0 \approx 35$ K), and of the temperature at which the energies for both phases equal ($T_C = T_0 + \Delta T \approx 166$ K). That would be the critical temperature in a controlled experiment on a single crystal, which agrees

with the proposed critical temperature of Gibbs *et al.* [41]. In our experiments, since we deal with ceramic materials, and once the ferroelastic transition occurs by nucleation of domains containing distorted cells, the transition temperature probably decreased because of the influence of defects, which generate strain fields, favoring the distorted monoclinic structure.

IV. CONCLUSIONS

Ba_2ZnTeO_6 undergoes a structural phase transition (SPT) at around 140 K. The SPT has a first-order character, with a small entropy jump characteristic of a displacive transition (driven by the condensation of a vibrational mode). Raman and infrared spectra are compatible with a SPT by lowering the symmetry from the room-temperature rhombohedral structure ($R\bar{3}m$ space group) to a monoclinic low-temperature one (belonging to the $C2/m$ space group). This ferroelastic transition is then accompanied by the appearance of an (in-plane) elastic distortion, which is seen in the spectra by raising the degeneracy of doubly degenerate E-type modes. A clear soft-mode behavior, confirming the displacive nature of the transition, was found for the rhombohedral $E_g(1)$ Raman mode, which splits into $A_g(1) + B_g(1)$ modes of the monoclinic structure, both presenting soft-mode behavior. Using complementary Raman-polarized measurements, group theoretical tools, and group-to-subgroup correlation tables, all the relevant phonon features for both structures were identified and assigned to their correct symmetries.

ACKNOWLEDGMENTS

The authors acknowledge the financial support from the following agencies: Coordenação de Aperfeiçoamento de Pessoal de Nível Superior (CAPES); Conselho Nacional de Desenvolvimento Científico e Tecnológico (CNPq); Financiadora de Estudos e Projetos (FINEP); and Fundação de Amparo à Pesquisa do Estado de Minas Gerais (FAPEMIG). R.L.M. thanks ESPCI for an invited "Chaire Joliot" appointment. The Laboratory of Crystallography (LabCri) of the Department of Physics of UFMG is also acknowledged for providing equipment and technical support for structural characterizations.

[1] Y. Saito, H. Takao, T. Tani, T. Nonoyama, K. Takatori, T. Homma, T. Nagaya, and M. Nakamura, Nature (London) **432**, 84 (2004).
[2] T. Takenaka, H. Nagata, and Y. Hiruma, Jpn. J. Appl. Phys. (Pt. 2) **47**, 3787 (2008).
[3] K.-I. Kobayashi, T. Kimura, H. Sawada, K. Terakura, and Y. Tokura, Nature (London) **395**, 677 (1998).
[4] J. Suntivich, K. J. May, H. A. Gasteiger, J. B. Goodenough, and Y. Shao-Horn, Science **334**, 1383 (2011).
[5] Y. H. Huang, R. I. Dass, Z. L. Xingand, and J. B. Goodenough, Science **312**, 254 (2006).
[6] J. Wang, J. B. Neaton, H. Zheng, V. Nagarajan, S. B. Ogale, B. Liu, D. Viehland, V. Vaithyanathan, D. G. Schlom, U. V. Waghmare, N. A. Spaldin, K. M. Rabe, M. Wuttig, and R. Ramesh, Science **299**, 1719 (2003).
[7] W. Eerenstein, N. D. Mathur, and J. F. Scott, Nature (London) **442**, 759 (2006).
[8] A. W. Sleight, J. L. Gillson, and P. E. Bierstedt, Solid State Commun. **17**, 27 (1975).
[9] S. Vasala and M. Karppinen, Prog. Solid State Chem. **43**, 1 (2015).
[10] T. Aoba, T. Tiittanen, H. Suematsu, and M. Karpinen, J. Solid State Chem. **233**, 492 (2016).
[11] H.-J. Von Rother, S. Kemmler-Sack, and A. Fadini, Z. Anorg. Allg. Chem. **436**, 213 (1977).
[12] P. Von Köhl, U. Müller, and D. Reinen, Z. Anorg. Allg. Chem. **392**, 124 (1972).
[13] G. M. Keith, C. A. Kirk, K. Sarma, N. McN. Alford, E. J. Cussen, M. J. Rosseinsky, and D. C. Sinclair, Chem. Mater. **16**, 2007 (2004).
[14] S.-F. Wang, Y.-F. Hsu, H.-S. Huang, and Y.-J. Liu, Ceram. Int. **37**, 1327 (2011).
[15] M. Retuerto, J. A. Alonso, M. J. Martínez-Lope, M. García-Hernández, K. Krezhov, I. Spirov, T. Ruskov, and M. T. Fernández-Díaz, Eur. J. Inorg. Chem. **2008**, 2286 (2008).
[16] F. Sher and J. P. Attfield, Solid State Sci. **8**, 277 (2006).
[17] G. Blasse, J. Inorg. Nucl. Chem. **27**, 993 (1965).
[18] H. L. Feng, P. Adler, M. Reehuis, W. Scnelle, P. Pattison, A. Hoser, C. Felser, and M. Jansen, Chem. Mater. **29**, 886 (2016).
[19] P. Kayser, S. Injac, B. Ranjbar, B. J. Kennedy, M. Avdeev, and K. Yamaura, Inorg. Chem. **56**, 9009 (2017).
[20] C. P. Khattak, D. E. Cox, and F. F. Y. Wang, in *20th Annual Conference on Magnetism and Magnetic Materials, San Francisco*, edited by C. D. Graham, Jr., G. H. Lander, and J. J. Rhyne, AIP Conf. Proc. No. 24 (AIP, New York, 1974), p. 68.
[21] H. U. Schaller and S. Kemmler-Sack, Z. Anorg. Allg. Chem. **473**, 178 (1981).
[22] U. Treiber and S. Kemmler-Sack, Z. Anorg. Allg. Chem. **470**, 95 (1980).
[23] M. Liegeois-Duyckaerts, Spectrochim. Acta A **41**, 523 (1985).
[24] S. A. Ivanov, P. Nordblad, R. Mathieu, R. Tellgren and C. Ritter, Dalton Trans. **39**, 5490 (2010).
[25] R. Mathieu, S. A. Ivanov, R. Tellgren, and P. Nordblad, Phys. Rev. B **83**, 174420 (2011).
[26] B. J. Kennedy, C. J. Howard, K. S. Knight, Z. Zhang, and Q. Zhou, Acta Cryst. B **62**, 537 (2006).
[27] M. C. Castro Jr., E. F. V. Carvalho, W. Paraguassu, A. P. Ayala, F. C. Snyder, M. W. Lufaso, and C. W. A. Paschoal, J. Raman Spectrosc. **40**, 1205 (2009).
[28] P. J. Saines, J. R. Spencer, B. J. Kennedy, and M. Avdeev, J. Solid State Chem. **180**, 2991 (2007).
[29] M. V. Gorev, I. N. Flerov, and Ph. Sciau, Phys. Solid State **43**, 345 (2001).
[30] S. A. Ivanov, P. Nordblad, R. Mathieu, R. Tellgren, and C. Ritter, Dalton Trans. **39**, 11136 (2010).
[31] S. A. Larrégola, J. A. Alonso, D. Sheptyakov, M. Algueró, A. Muñoz, V. Pomjakushin, and J. C. Pedregosa, J. Am. Chem. Soc. **132**, 14470 (2010).
[32] A. S. Gibbs, K. S. Knight, P. J. Saines, J. R. Hester, and H. Takagi, Acta Cryst. A **72**, s62 (2016).
[33] A. S. Gibbs, A. Yamamoto, A. N. Yaresko, K. S. Knight, H. Yasuoka, M. Majumder, M. Baenitz, P. J. Saines, J. R. Hester,

D. Hashizume, A. Kondo, K. Kindo, and H. Takagi, Phys. Rev. B **95**, 104428 (2017).

[34] A. Dias, G. Subodh, M. T. Sebastian, and R. L. Moreira, J. Raman Spectrosc. **41**, 702 (2009).

[35] K. G. Sudarsan and S. N. Dindi, Prog. React. Kinet. Mech. **27**, 127 (2002).

[36] C. C. Homes, M. Reedyk, D. A. Crandles, and T. Timusk, Appl. Opt. **32**, 2976 (1993).

[37] See Supplemental Material at http://link.aps.org/supplemental/10.1103/PhysRevMaterials.2.054406 for XRD patterns, DSC data, and detailed temperature evolution of the phonon frequencies in the range of the structural phase transition.

[38] D. L. Rousseau, R. P. Bauman, and S. P. S. Porto, J. Raman Spectrosc. **10**, 253 (1981).

[39] F. Gervais and P. Echegut, *Infrared Studies of Incommensurate Systems, in Incommensurate Phases in Dielectrics–Fundamentals*, edited by R. Blinc and A. P. Levanyuk (North-Holland, Amsterdam, 1986), pp. 337–364.

[40] M. Balkanski, *Optical Properties due to Phonons, in Handbook on Semiconductors*, edited by T. S. Moss and M. Balkanski (North-Holland, Amsterdam, 1980), Vol. 2, pp. 497–543.

[41] A. F. Corsmit and G. Blasse, J. Inorg. Nucl. Chem. **36**, 1155 (1974).

[42] K. P. F. Siqueira, R. L. Moreira, and A. Dias, Chem. Mater. **22**, 2668 (2010).

[43] A. Dias, M. M. Lage, L. A. Khalam, M. T. Sebastian, and R. L. Moreira, Chem. Mater. **23**, 14 (2011).

[44] B. A. Strukov and A. P. Levanyuk, *Ferroelectric Phenomena in Crystals: Physical Foundations* (Springer-Verlag, Berlin, 1998), p. 159.

[45] K. Aizu, J. Phys. Soc. Jpn. **27-2**, 387 (1969).

[46] Bilbao crystallographic server at www.cryst.ehu.es.

[47] J. L. Birman, Phys. Lett. A **45**, 196 (1973).

[48] P. A. Fleury, J. F. Scott, and J. M. Worlock, Phys. Rev. Lett. **21**, 16 (1968).

[49] J. C. Toledano and P. Toledano, *The Landau Theory of Phase Transitions* (World Scientific, Singapore, 1987).